Real-space Green's function approach for x-ray spectra at high temperature

Tun S. Tan, J. J. Kas, and J. J. Rehr*
Department of Physics, University of Washington, Seattle, Washington 98195-1560, USA

(Received 12 March 2021; revised 2 June 2021; accepted 12 July 2021; published 23 July 2021)

There has been considerable interest in properties of condensed matter at high temperature, including nonequilibrium behavior and extreme conditions up to the warm dense matter regime. Such behavior is encountered, e.g., in experimental time-resolved x-ray absorption spectroscopy in the presence of intense laser fields. In an effort to simulate such behavior, we present an approach for calculations of high-temperature x-ray absorption spectra in arbitrary materials, using a generalization of the real-space Green's function formalism. The method is incorporated as an option in the core-level x-ray spectroscopy code FEFF10. To illustrate the approach, we present calculations for several materials together with comparisons to experiment and with other methods.

DOI: 10.1103/PhysRevB.104.035144

I. INTRODUCTION

X-ray absorption spectroscopy (XAS) has become an important tool for studies of materials in fields ranging from materials science and chemistry to geophysics and astrophysics [1–6]. XAS is used extensively to probe both local electronic and structural properties simultaneously at synchrotron facilities worldwide. With the development of x-ray free electron lasers (XFELs), XAS experiments have been extended to treat ultrashort femtosecond to picosecond timescales and nonequilibrium conditions, with temperatures T up to many thousands of K. These capabilities are important, e.g., for studies of matter in extreme conditions as well as nonequilibrium and dynamic response due to electron-phonon energy transfer, spin relaxation, reactions, and in shocked matter. The extreme conditions include the warm dense matter (WDM) regime, where $T \sim T_F$, the Fermi temperature, which is typically a few $\times 10^4$ K, and the density is within an order of magnitude or so of normal conditions.

Modern theories of optical and x-ray spectra start from the many-body Fermi's golden rule, but are usually cast at zero temperature. In order to make the calculations computationally tractable, a single-particle or quasiparticle approximation for the photoelectron is often used [7,8]. Although many density functional based codes have the capability to perform calculations at finite temperatures, there is an inherent limitation to relatively low temperatures, due to the high computational cost of calculating states at high energies, well above the chemical potential. At very high temperatures, i.e., in the warm dense matter (WDM) regime, the multiple scattering (MS) or Korringa-Kohn-Rostoker (KKR) methods have an advantage over other approaches due to the efficient calculation of high-energy states. Recent developments in the past few years have shown great promise in predicting high-temperature electronic structure and equations of state, for example [9–11]. In this paper, we describe developments to the real-space multiple-scattering code FEFF to include a variety of high-temperature effects, with a focus on calculations of both excited-state electronic structure and x-ray spectra.

The quasiparticle approximation is the basis of the real-space Green's function (RSGF) approach used in the FEFF codes [12], which are applicable to systems throughout the periodic table. However, heretofore the code neglects FT effects other than thermal vibrations and is limited to relatively low temperatures (LT), defined here as the regime with temperature T below a few times the Debye temperature T_D, which is of order a few hundred K. Our main aim in this work is to extend the RSGF approach for SCF electronic structure and XAS to high temperature (HT), defined here as the range from a few T_D up to the WDM regime where $T \sim T_F$. Second, we aim to explore both HT and nonequilibrium behavior of x-ray spectra in a few systems that can be measured experimentally. The generalization of the RSGF approach to HT requires a number of extensions since many ingredients, e.g., the chemical potential, exchange-correlation potential, quasiparticle self-energy, and mean-free path exhibit significant temperature dependence at HT. Vibrational effects also require special treatment at HT. In nonequilibrium conditions it may be necessary to treat both electronic temperature T_e and lattice temperature T_L separately. While FT theories have been developed previously for some of these effects, e.g., self-consistent field (SCF) electronic structure [13,14], many other FT developments [15–17] are intended for LT applications, where T is at most few hundred K. In contrast, our approach here is intended to provide an integrated treatment of all important FT behavior, both LT and HT in both electronic structure and x-ray spectra, within a generalized RSGF workflow. For $T_e \ll T_F$, the exchange-correlation potential and self-energy are weakly temperature dependent, so that a zero-electronic-temperature approximation may be adequate for electronic components. However, in the WDM regime where $T \sim T_F$, an explicit account of electronic-temperature dependence is necessary since the exchange-correlation potential in WDM varies from exchange- to correlation-dominated behavior with increasing temperature [18]. As for $T = 0$, an efficient

*jjr@uw.edu

approximation for the XAS cross section can be obtained at any T using the RSGF formalism [9,10], which is the real-space analog of the KKR band structure approach [19]. This approach is based on the one-particle electron Green's function, which can be calculated either by matrix inversion or by a well-converged multiple-scattering path expansion. Our current FT implementation builds upon the theory and algorithms used in the FEFF9 code [12], and has been incorporated in a new version FEFF10 [20]. This theory is illustrated here with a number of examples. While the theory is generally applicable to systems throughout the periodic table, we focus on applications at normal pressures and densities, where the theory can be tested against recent experiments.

The remainder of the paper is organized as follows: In Sec. II. we briefly review the XAS theory and the RSGF formalism. Section III. enumerates the HT effects, and Sec. IV. presents a number of examples. Finally, Sec. V. contains a brief summary and conclusions.

II. XAS THEORY AT $T = 0$

A. Fermi golden rule

In this section, we briefly summarize the theory of x-ray absorption spectra based on the RSGF approach at $T = 0$. Theories of the XAS cross section typically start from the many-body Fermi golden rule

$$\sigma(\omega) = 4\pi^2 \frac{\omega}{c} \sum_F |\langle I|\hat{D}|F\rangle|^2 \delta(\omega + E_I - E_F), \tag{1}$$

where $|I\rangle$ is the many-body ground state of the system with total energy E_I, $|F\rangle$ ranges over the many-body final states with energy E_F, and $\hat{D}$ is the many-body transition operator due to the x-ray field, which here is taken to be a dipole interaction $D = \Sigma_{i,f} d_{ij} \hat{c}_f^\dagger \hat{c}_i$ where d_{ij} are the dipole matrix elements, and c_i and $c_i^\dagger$ are electron annihilation and creation operators, respectively. Here and throughout this paper we use atomic units $e = \hbar = m = 1$, and temperatures in eV (1 eV $= 11\,604$ K), unless noted otherwise. In order to reduce the calculation to a single-particle framework, we make a sudden approximation as in the ΔSCF approximation, with the final-state rule [21]. Since a core electron leaves behind a hole after being excited into the photoelectron state the final photoelectron state $|\phi_f\rangle$ must take into account the interaction with the core hole potential, while a given core level $|\phi_i\rangle$ is calculated with the initial state configuration. Next, the many-particle initial and final states are factored such that $|I\rangle = |\phi_i\rangle|\Phi_0^{N-1}\rangle$ and $|F\rangle = |\phi_f\rangle|\tilde{\Phi}_n^{N-1}\rangle$, where $|\tilde{\Phi}_n^{N-1}\rangle$ is the nth excited state of the $N-1$ electron system with a core hole in level i, and $|\phi_f\rangle$ is the photoelectron state calculated in the presence of the core hole. If one ignores the energy dependence of excitations of the $N-1$ electron system, Eq. (1) yields an effective zero-temperature single-particle cross section $\sigma_1(\omega)$:

$$\sigma_1(\omega) = 4\pi^2 \frac{\omega}{c} \sum_i^{occ} \sum_f |\langle i|\hat{d}|f\rangle|^2 \delta_\Gamma(\omega + \varepsilon_i - \varepsilon_f). \tag{2}$$

Here ε_i and ε_f are the eigenenergies of the quasiparticle initial $|i\rangle$ (deep-core) and final $|f\rangle$ (photoexcited) states, and $\delta_\Gamma(\omega)$ denotes a Lorentzian of width Γ, where Γ includes the core-hole lifetime broadening. More generally this approximation can be corrected to include shakeup effects by a convolution of the single-particle XAS with the core spectral function, defined as $A_c(\omega) = \Sigma_n S_n^2 \delta(\omega - \omega_n)$ where $S_n^2 = |\langle \Phi_0^{N-1}|\tilde{\Phi}_n^{N-1}\rangle|^2$ is the many-body amplitude overlap integral between initial and final states. This convolution modifies the cross section by an additional, energy-dependent broadening factor [22] of unit weight which damps the fine structure by a constant factor historically denoted by S_0^2 [23].

B. Real-space Green's function approach

A significant advantage of the RSGF formalism is that it implicitly builds in the summation over final states f, which is a computational bottleneck in wave-function approaches at high energies [12]. In addition, it builds in the coupling between the photoelectron and the solid, in terms of an energy-dependent photoelectron self-energy $\Sigma(\varepsilon)$, where $\varepsilon = \omega + \varepsilon_i$ is the photoelectron energy. Formally the retarded single-electron Green's function $G(\varepsilon)$ in a basis of local site-angular momentum states $|Lj\rangle$ [23] can be defined by the spectral sum

$$\begin{aligned} G_{Lj,L'j'}(\varepsilon) &= \langle Lj|G(\varepsilon)|L', j'\rangle \\ &= \sum_f \frac{\langle Lj|f\rangle\langle f|L'j'\rangle}{\varepsilon - \varepsilon_f + i\eta}, \end{aligned} \tag{3}$$

where j is the index for a given site $\mathbf{R}_j$ and $L = (l, m)$ are the angular momentum quantum numbers. Here ε_f is the eigenvalue of the final-state quasiparticle Hamiltonian $H = p^2/2 + v_f + \Sigma(\varepsilon)$, v_f the SCF Hartree potential of the final state in the presence of a core hole, and $\Sigma(\varepsilon)$ is the dynamically screened self-energy that replaces the one-particle eigenstates with quasiparticle levels denoted by a subscript qp. The basis states $|L, j\rangle = j_l(kr)Y_L(\hat{r})$ where $j_l(kr)$ is a spherical Bessel function, $Y_L(\hat{r})$ a spherical harmonic, and $k = [2(\varepsilon - \varepsilon_F)]^{1/2}$ is the photoelectron wave number relative to the Fermi energy threshold ε_F. The key ingredients in the RSGF calculation of G are matrix elements of the free Green's function $G^0_{Lj,L'j'} = G^0_{L,L'}(\mathbf{R}_j - \mathbf{R}_{j'})$ and the full scattering T matrix $T_{Lj,L'j'} = t_{lj}\delta_{j,j'}\delta_{L,L'}$, where $t_{lj} = \exp(i\delta_{lj})\sin\delta_{lj}$. The partial-wave phase shifts δ_{lj} due to the spherical scattering potential $v(r_j)$ at a given site j, where $r_j = |\mathbf{r} - \mathbf{R_j}|$, are obtained by matching the outgoing part of the radial solution of the Dirac equation $R_l(r) = R_l^+(r) + cc$ at that site to outgoing free spherical Hankel functions $h_l^{(1)}(kr)$ at the muffin-tin radius $R_l^+(r) = h_l^{(1)}(kr)\exp(i\delta_l)$. Multiple scattering of the photoelectron by its environment is naturally built into the RSGF formalism [24]. Contributions from the central absorbing atom $j = 0$ and the neighboring scatterers are separated by defining $G = G^c + G^{sc}$. The scattering contributions in G^{sc} are obtained from the matrix inverse solution to the Dyson equation [21,24], which builds in multiple scattering to all orders:

$$G^{sc}_{L0,L'0} = e^{i\delta_{l0}}[(1 - \bar{G}^0 T)^{-1}\bar{G}^0]_{L0,L'0}e^{i\delta_{l'0}}. \tag{4}$$

Here $\bar{G}^0_{Lj,L'j'} = (1 - \delta_{j,j'})G^0_{Lj,L'j'}$ and for simplicity we have dropped the subscripts $Lj, L'j'$ on matrix elements of $\bar{G}^0$ and T and the site index j on the phase shifts δ_{lj} except

where needed for clarity. The absorbing atom part G^c is obtained from the regular $R_L(\mathbf{r})$ and outgoing $R_L^+(\mathbf{r})$ solutions of the Dirac equation at the absorbing atom $j = 0$, and satisfies $\mathrm{Im}\, G^c_{L0,L'0} = -\pi\delta_{L,L'}$. For extended x-ray absorption fine structure (EXAFS) energies (typically above about 20–30 eV of an absorption edge), the matrix inverse in Eq. (4) can be expanded in a rapidly converging series of scattering paths typically with less than four legs. However, for x-ray absorption near-edge structure (XANES), full multiple scattering (FMS) is usually needed and can be carried out by a fast matrix inversion algorithm since the basis of relevant angular momenta and sites is small due to the short mean-free path and small $l_{\max} < 4$. By inserting the spectral representation of $G(\varepsilon)$ into Eq. (2) together with Fermi-Dirac occupation numbers, the final states are implicitly summed in the calculation of the cross section $\sigma^0_{qp}(\omega)$ [24],

$$\sigma^0_{qp}(\omega) = -4\pi\frac{\omega}{c}\,\mathrm{Im}\sum_{i}^{occ}\sum_{LL'}\langle i|\hat{d}\; G_{L0,L'0}(\omega+\varepsilon_i)\;\hat{d}^\dagger|i\rangle \times\theta(\omega+\varepsilon_i-\varepsilon_F), \tag{5}$$

where ε_F is the Fermi energy and θ the unit step function. Core-hole lifetime broadening is added at the end of the calculation by convolution with a Lorentzian function $\delta_\Gamma(\omega)$, yielding a net XAS

$$\sigma_{qp}(\omega) = \delta_\Gamma(\omega) * \sigma^0_{qp}(\omega). \tag{6}$$

III. FINITE-TEMPERATURE SCF AND XAS

A number of effects come into play in the theory of SCF electronic structure and XAS at finite temperature. While some of these can be neglected in the LT regime, all can be important at HT. First, the RSGF expression for the XAS must take into account the Fermi occupation numbers of the core and unoccupied states. Second are effects of electronic temperature due to the temperature dependence of the electron density and chemical potential. Third there are FT effects on exchange and correlation, both through the exchange-correlation potential v_{xc} and the quasiparticle self-energy $\Sigma(\varepsilon)$, which become important only when T is of order the Fermi temperature T_F. Finally, there are the FT effects of lattice vibrations that strongly damp the XAS fine structure at all temperatures. These effects are summarized in more detail below:

(1) First, much of the electronic-temperature dependence in the spectra is due to that in the occupation numbers of the initial and final states. To account for this effect, the RSGF expression for the XAS must be generalized to include the Fermi-factor occupation numbers f_T and $1 - f_T$ for the occupied and unoccupied levels, respectively,

$$\sigma^0_{qp}(\omega, T) = -4\pi\frac{\omega}{c}\,\mathrm{Im}\sum_{iLL'}\langle i|\hat{d}\; G_{L0,L'0}(\omega+\varepsilon_i)\;\hat{d}^\dagger|i\rangle \times f_T(\varepsilon_i)[1-f_T(\omega+\varepsilon_i)], \tag{7}$$

where $f_T(\varepsilon) = 1/\{\exp[(\varepsilon-\mu)/k_BT]+1\}$, $\mu(T)$ is the chemical potential of the system, and site 0 is taken to be the absorbing atom. A consequence is that the x-ray "edge" of the cross section is modified by a Fermi-function cutoff which broadens by an amount of order k_BT with increasing T.

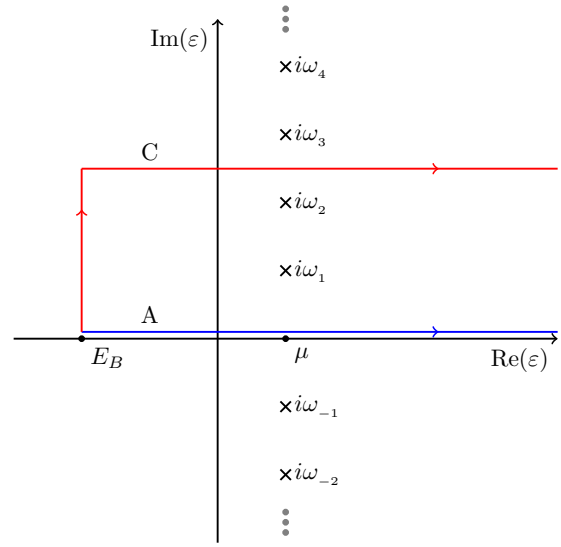

FIG. 1. Energy contour for electron density calculation at finite temperature: $\omega_j = \pi(2j-1)k_BT$ denotes the imaginary part of the Matsubara poles of the Fermi function $f_T(\varepsilon)$. The integration starts from some core-valence separation level E_B above the core states but below the valence states. Contour A (blue) represents the original integration path just above the real axis, while contour C (red) represents the integration path in the complex plane.

(2) FT SCF: As for $T = 0$ in order to construct the FT electron density and (scattering) potentials $v(r)$, we implement a generalization of the self-consistent field (SCF) method to calculate the Coulomb potentials, electron densities, and a temperature-dependent chemical potential. In the RSGF approach in FEFF, the SCF procedure starts with the overlapped atomic electron densities obtained by solving the relativistic Dirac-Fock equations for each atom in the system. From this initial guess of the electron density, a Green's function is calculated, which provides a new density and chemical potential. This procedure is then repeated until self-consistency ($\rho_i = \rho_{i-1}$) is reached to high accuracy, typically in about 20 iterations or so. Assuming a frozen core, the valence electron contribution to density of electrons is given in terms of an integral over energy of the imaginary part of the Green's function,

$$\rho(\mathbf{r}) = -\frac{2}{\pi}\int_{E_B}^{\infty} d\varepsilon\;\mathrm{Im}\;G(\mathbf{r},\mathbf{r},\varepsilon)f_T(\varepsilon), \tag{8}$$

where E_B is the core-valence separation energy (typically set to -40 eV in FEFF), and the factor of 2 accounts for spin degeneracy. For computational efficiency at both zero and finite temperatures, the above integral is carried out in the complex plane where the Green's function becomes smooth, similar to the approach of Zeller [13]. We integrate along a contour C (shown in Fig. 1), where the first leg traverses from E_B to $E_B + i2\pi nk_BT$, then to $+\infty + i2\pi nk_BT$, where $i2\pi nk_BT$ is halfway between the Matsubara poles. For a given chemical potential, the valence density is then

given by

$$\rho(\mathbf{r}) = -\frac{2}{\pi}\mathrm{Im}\left[\int_C d\varepsilon\, G(\mathbf{r},\mathbf{r},\varepsilon) f_T(\varepsilon), \right.$$
$$\left. - i2\pi k_B T \sum_{j=1}^{n} G(\mathbf{r},\mathbf{r},z_j)\right], \tag{9}$$

where $z_j = \mu \pm i\pi(2j-1)k_BT$ are the Matsubara poles, and n is the number of poles between the contour C and the real axis. Equation (9) also has implicit dependence on the chemical potential through the Fermi function. In turn, the chemical potential is found by enforcing charge neutrality

$$N_e = \int d^3r\, \rho(\mathbf{r};\mu(T)), \tag{10}$$

where N_e is the number of valence electrons in the system, again treating the core electrons as frozen. Equations (5) and (7) for the cross section contain similar integrals of the Green's function multiplied by the Fermi function in order to include the core-hole broadening. These integrals are dealt with in a similar manner, although the contour is slightly different, in principle extending from $-\infty + i2\pi nk_BT$ to $+\infty + i2\pi nk_BT$. There is also an additional pole arising from the Lorentzian lifetime broadening function $\delta_\Gamma(\omega)$ which has poles at $\pm i\Gamma$.

(3) FT exchange-correlation potentials: Additional temperature dependence comes from that in the exchange-correlation potentials (which affect the initial state densities and potentials) which is most significant at HT. An approach for calculating these exchange-correlation potentials from first principles with a FT cumulant Green's function approach has been discussed by Kas *et al.* [18], which shows that the potentials cross over from exchange to correlation dominated with increasing T. Here, the behavior is treated by an efficient parametrized extension of DFT fit to quantum Monte Carlo calculations (QMC) by Karasiev, Sjostrom, Dufty, and Trickey (KSDT) [25], which agrees well with the FT cumulant results of Kas *et al.* [18].

(4) FT self-energy effects: The temperature dependence of the dynamical quasiparticle self-energy also becomes significant at HT in calculations of the quasiparticle photoelectron states, and hence the transition matrix elements at energies above an edge. In the HT regime, the self-energy is smoothly varying with energy and roughly approximated by a constant that adds additional broadening to the spectra. Since full calculations of the FT self-energy [26] are computationally demanding, we have developed a more efficient FT COHSEX approximation to the *GW* self-energy for this purpose [27].

(5) Lattice vibrations: At any temperature, lattice vibrations exponentially damp electron scattering with increasing energy. Approximate calculations in the LT regime can be done by including appropriate Debye-Waller factors $\exp(-2\sigma^2k^2)$ for each multiple scattering path in the multiple-scattering path expansion, or in the bare Green's function propagator G_0 for for full-multiple-scattering (FMS) calculations. This can be done using the path-dependent correlated Debye model with mean-square radial displacements $\sigma^2(T) \propto T/T_D$, where T_D is the Debye temperature. For FMS, this approximation with the near neighbor $\sigma^2(T)$ agrees with

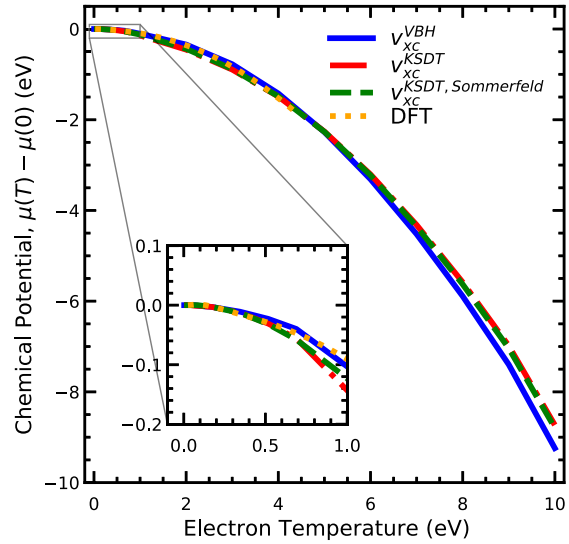

FIG. 2. Chemical potential shift for fcc aluminum $\mu(T_e) - \mu(0)$ versus electronic temperature T_e at normal density $r_s = 2.07$ using the ground-state von Barth–Hedin [29] (blue) and finite-T KSDT [25] (red) exchange-correlation potentials. For comparison, a DFT calculation of the chemical potential using the Sommerfeld expansion that ignores self-energy effects [30] (orange) is also shown up to $T_e = 4$ eV. The result with the Sommerfeld expansion (green) is shown for the KSDT exchange-correlation potential. The inset shows the chemical potential shift up to $T_e = 1$ eV.

that for the dominant, single-scattering term. Further details are given in Ref. [28]. However, this approach may be inapplicable in the near-edge regime where symmetry breaking occurs, and at HT $T \gg T_D$, where the quasiharmonic approximation breaks down.

For these HT cases a configurational average over an ensemble of distorted structures at a given temperature is called for. For example, in the HT regime one can use auxiliary finite-T quantum molecular dynamics (QMD) to obtain a temperature-dependent configurational average of the spectrum. Closer to zero temperature, zero-point motion can also be included via quantum Monte Carlo (QMC) sampling.

IV. EXAMPLE CALCULATIONS

A. Simple metal: Al

Aluminum (fcc Al) is a prototypical nearly free-electron system for testing electronic-structure calculations. The electronic density of states (DOS) for Al in the conduction band is similar to that for a free-electron model, with a square-root-like dispersion at the bottom of the band, a density parameter $r_s = 2.07$ and Fermi temperature 13.7×10^4 K $= 11.7$ eV at normal conditions. We highlight the effect of FT exchange-correlation potentials on the chemical potential shift for Al in Fig. 2. We computed the chemical potential shift using the ground-state von Barth–Hedin (v_{xc}^{VBH}) exchange-correlation potential [29] and the FT approximation v_{xc}^{KSDT} of KSDT [25] for electronic temperatures T_e up to $T_e = 10$ eV or about 10^5 K.

Our calculation of the chemical potential with v_{xc}^{VBH} agrees well with that of Lin *et al.* [30] up to $T_e = 4$ eV, and is reasonably accurate up to about 10 eV, consistent with the

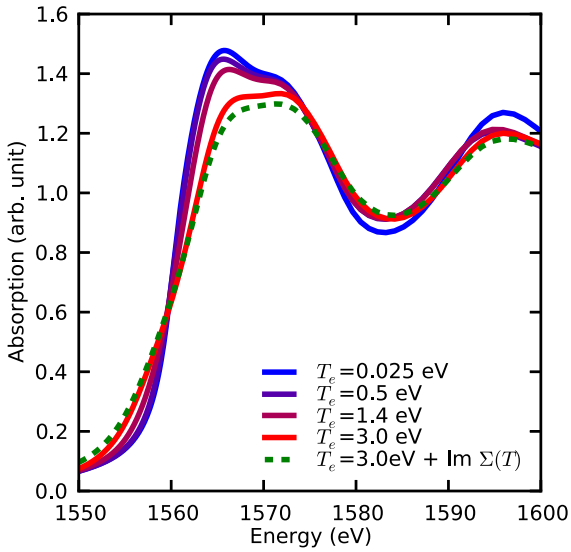

FIG. 3. K-edge XAS for fcc Al vs electronic temperature T_e at normal density ($r_s = 2.07$) including the FT SCF, Fermi occupation factors, and the finite-T KSDT exchange-correlation potential, but ignoring vibrational effects (see text). The effect of the FT self-energy is found to give an additional 0.5 eV broadening at $T_e =$ 3.0 eV (green dashed). Note that the edge broadens considerably with increasing T_e, mostly due to the smearing of the Fermi function.

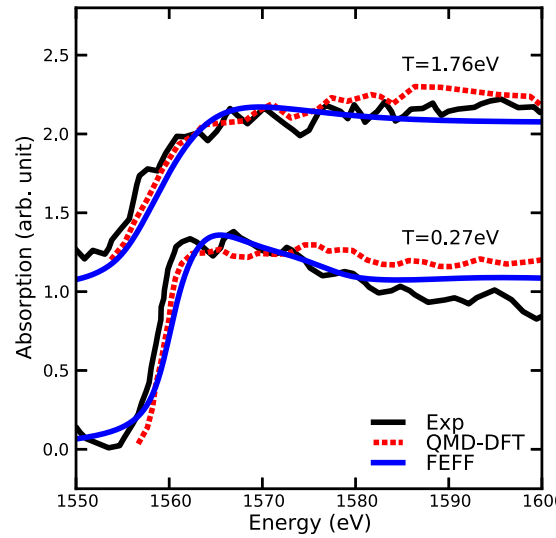

FIG. 4. Calculated K-edge XAS for equilibrium Al ($T_e = T_L$) at normal density ($r_s = 2.07$) vs experimental XAS at $T = 0.27$ and 1.76 eV. From bottom to top, QMD-DFT [31] are simulated at $T =$ 0.43 and 2.6 eV while FEFF simulations are done at $T = 0.27$ and 3.0 eV. Note the substantial broadening of the edge with increased T, roughly consistent with experiment, and that lattice vibration effects completely damp the fine structure at HT. The fluctuations in the experimental XAS reflect experimental noise.

T_e^2 behavior of the Sommerfeld expansion. Remarkably the Sommerfeld expansion remains a good approximation even at very high T_e of order several eV.

Next, we investigate the electronic-temperature dependence of the K-edge XAS of Al at normal density up to WDM temperatures while fixing the atomic configuration. In our calculation, we account for the FT SCF, FT exchange-correlation potential, Fermi function smearing in the cross section, and finite lattice temperature. We show the calculated K-edge XAS for electronic temperatures $T_e = 0.025$, 0.5, 1.4, and 3.0 eV in Fig. 3, ignoring lattice temperature effects. The behavior at the edge is consistent with broadening of the Fermi distribution and the nearly free-electron density of states of Al. The "pre-edge" behavior of the XAS is due to the increasing contribution from previously occupied states below the $T_e = 0$ Fermi level. The FT correction to the chemical potential from $v_{\rm xc}^{\rm KSDT}$ is a secondary effect compared to the smearing of occupation at the Fermi level. The imaginary part of the self-energy, responsible for broadening in the spectrum, increases with temperature, while its variation in both the real and imaginary parts decreases [26]. The entire self-energy becomes structureless at very high temperatures. However, FT effects in the self-energy turn on slowly, and are appreciable compared to the other effects considered only at extreme temperatures $T \sim T_F$, well above those considered in this paper. To illustrate this, we show the XAS with and without the corresponding finite-temperature broadening of 0.5 eV at $T_e = 3.0$ eV in Fig. 3.

In addition to the two FT effects previously mentioned, we account for thermal vibrations in this example using the correlated Debye model ($T_D = 430$ K). We also contrast our FT RSGF calculation with the DFT-based XAS calculated using quantum molecular dynamics (QMD) structures averaged over several runs [31].

Investigations of the Al K edge under isochoric heating ($T_e = T_L$) at normal density ($r_s = 2.07$) were also done [31], with measurements at temperatures $T_e = T_L = 0.27$ and 1.76 eV, as in Fig. 4.

Our calculation with the correlated Debye model agrees fairly well with these results. The slope of the absorption edge is mainly due to the smearing of the Fermi function as illustrated in Fig. 3. The lattice vibration effect, which is included in the calculations shown in Fig. 4, attenuates the fine structure above the edge.

In principle, the correlated Debye model breaks down at high temperatures ($T_L > 0.27$ eV) when anharmonicity becomes large, but this is not a serious problem, as the fine structure in the XAS is largely suppressed at these high temperatures.

B. Warm dense Cu

Being a noble transition metal, fcc Cu has substantially different excited-state properties compared to simple nearly free-electron metals like aluminum. This is due to the highly localized d band just below the Fermi level. Hence, at elevated temperatures, the XAS also differs. Several works [4,32–34] studied these changes in the $L_{2,3}$ edge of Cu XAS in WDM using a more computationally expensive *ab initio* molecular dynamics (AIMD) simulation. Here we investigate the XAS of Cu using our FT SCF RSGF approach and the correlated Debye model. The electronic-temperature effects (FT SCF, FT $v_{\rm xc}$, and Fermi function in the cross section), and the lattice vibration effect on the $L_{2,3}$ edge are illustrated in Fig. 5. The simulated XANES spectra are computed at normal density

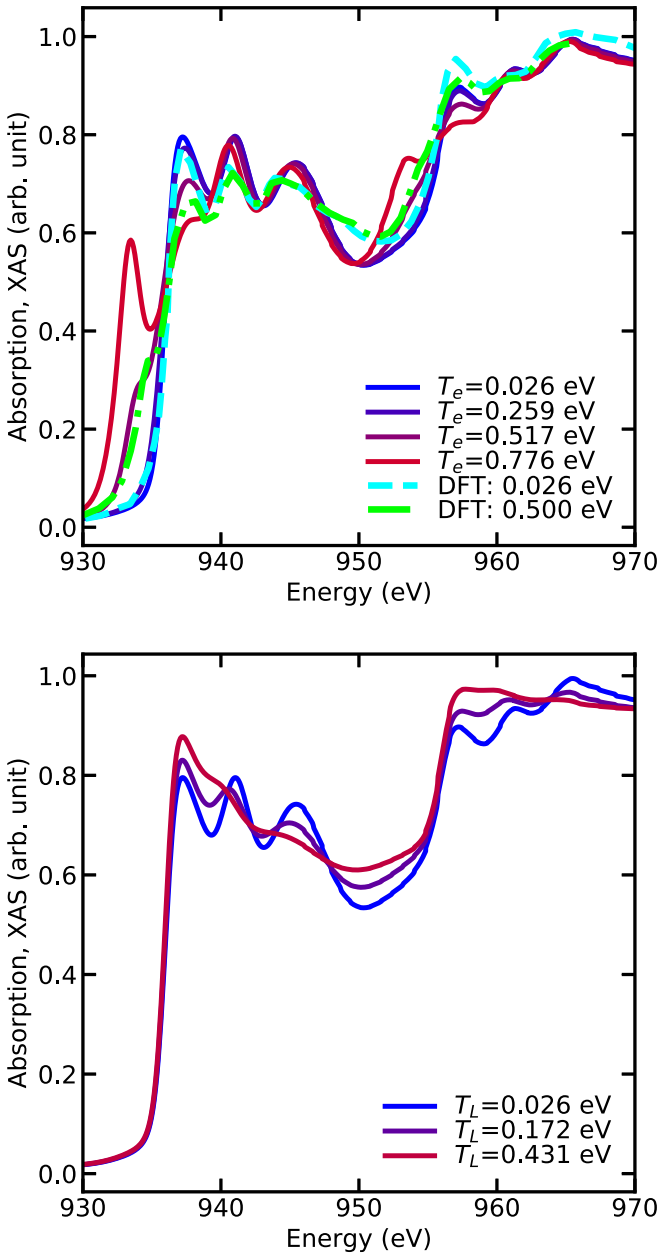

FIG. 5. Effect of electronic and lattice temperatures T_e and T_L on the L_3-edge XAS of fcc Cu at normal density ($r_s = 2.67$): (Top) T_e = 0.026 eV = 300 K up to 0.776 eV = 9000 K at T_L = 300 K. (Bottom) T_L = 0.026 eV = 300 K up to 0.431 eV = 5000 K at T_e = 300 K. The DFT calculation [35] is shown for T_e = 300 K (light blue) and for T = 0.5 eV = 5800 K (green).

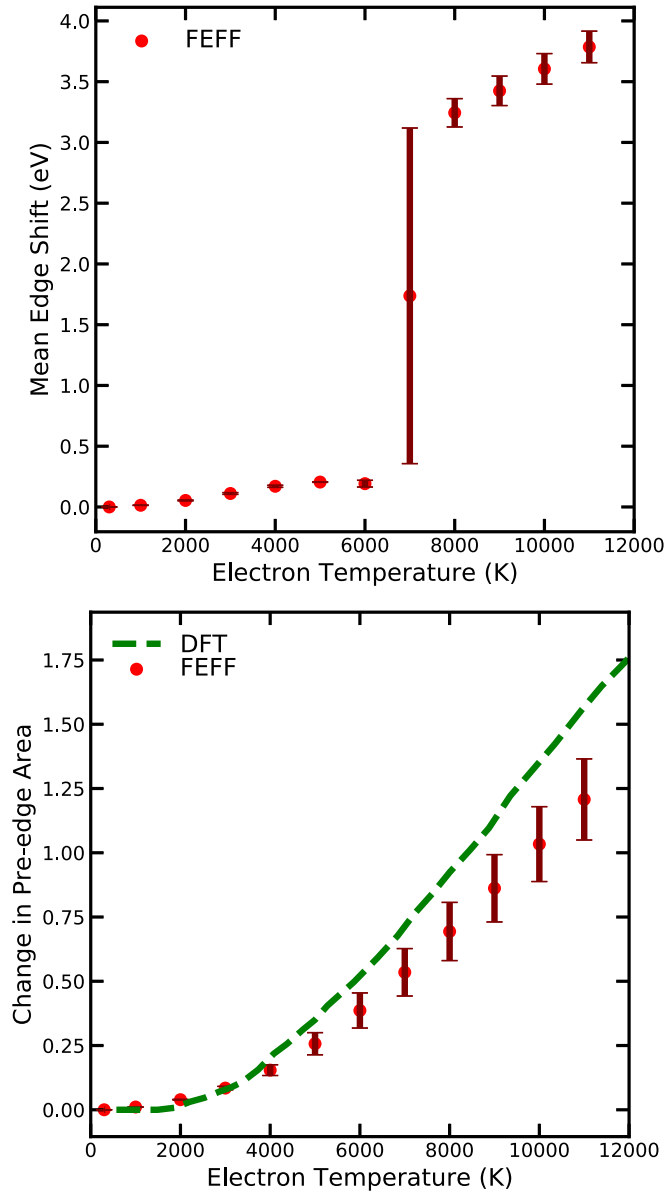

FIG. 6. (Top) Shift in the L_3 edge of fcc Cu at normal density ($r_s = 2.67$) as a function of electronic temperature (red); the sudden shift at about 7000 K is due to the onset of the d-band edge. (Bottom) Change in pre-edge area as a function of electronic temperature. The DFT calculation (green dashes) [35] was computed using ABINITat lattice temperature T_L = 300 K. Note that in contrast to the edge shift, the pre-edge area varies smoothly with temperature for Cu.

($r_s = 2.67$) for various temperatures. Our calculation is broadened with a Lorentzian to match that in the the DFT-based calculation [35]. As expected, the pre-edge structure in the XAS can be attributed to the increasing contribution from the d states below the $T = 0$ Fermi energy, as the Fermi distribution broadens significantly with increasing T_e [4,32–34]. Conversely, states just above the Fermi level have a reduced contribution leading to a smaller peak just above the edge. The changes in XAS due to electronic temperature are mainly localized in the near edge, whereas that due to the lattice temperature affects the region above the edge, especially the fine structure.

The edge shift and the pre-edge area are both possible candidates for assessing the internal temperature of a system. In order to extract the edge shift and pre-edge area, the edge position is defined to be the first local maximum of the first derivative in the XANES spectrum. The electronic-temperature dependence of the edge shift and pre-edge area are shown in Fig. 6. Note that the pre-edge area is monotonically increasing with the electronic temperature and it becomes linearly correlated to T_e above 6000 K, consistent with previous results [35]. In contrast, the edge shift is

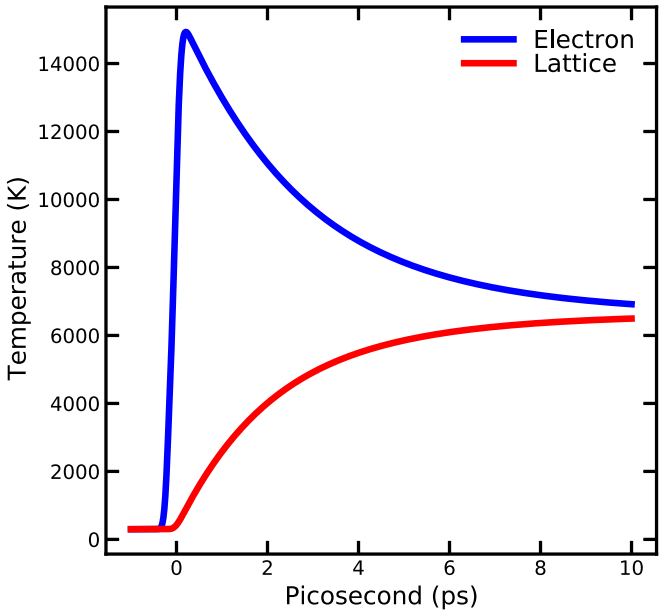

FIG. 7. Dynamics of electronic temperature T_e (blue) and lattice temperature T_L (red) of laser-pumped Cu based on two-temperature model calculation. The absorption power is calculated using the Beer-Lambert law with a Gaussian profile 400-nm laser source for a 70-nm-thick copper film.

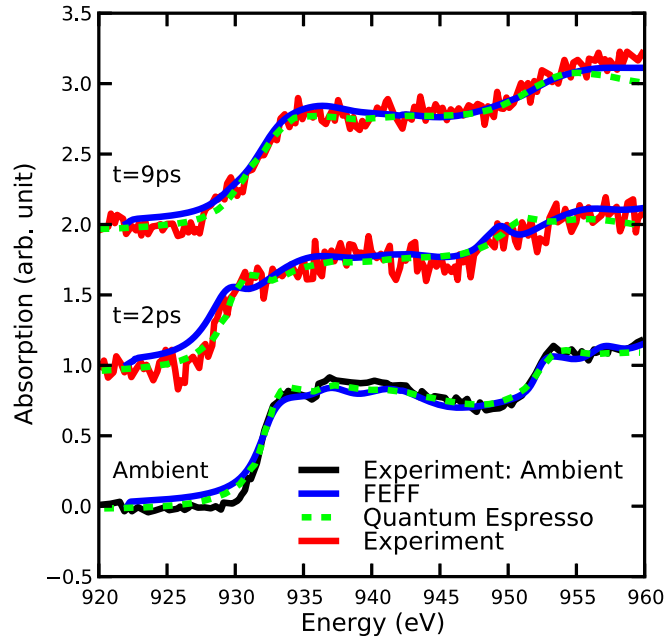

FIG. 8. Time-resolved XANES for 70 nm copper at different delay-times $t = 2$ ps and 9 ps. The experimental measurement (red) is averaged over 150 snapshots. The ambient condition measurement ($t = 300$ K) is averaged over 70 ps. Our calculations (blue) for delay-times $t = 2$ ps and 9 ps are computed at $T_e = 10\,200$ K and 6000 K, respectively, based on the two-T model results. The DFT results [4] (green) are calculated using the QUANTUM ESPRESSO code at the same temperatures.

highly nonlinear, exhibiting an abrupt shift at about 7000 K. Therefore, for Cu and probably for other transition metals as well, the pre-edge area is a better proxy for an electronic-temperature thermometer, compared to the edge shift.

Next, we compare our finite-temperature calculation to time-resolved, WDM experiments [4] in the context of nonequilibrium systems. The system being explored is a 70-nm copper foil heated optically by a 400-nm laser at a fluence of $0.33\,\mathrm{J/cm^2}$. As a consequence, the electrons are optically excited, leading to an initial huge pre-edge peak below the L_3 edge. The electronic and the lattice subsystems are out of equilibrium. In order to model the temperature evolution, we use a two-temperature ($2T$) model [4] with the same parameters for the electron heat capacity and electron-phonon coupling factor as in Zhibin *et al.* [30]. The temperature evolution is shown in Fig. 7. Note that the lattice temperature raises quickly above the melting temperature ~1358 K in under 1 ps due to the strong electron-phonon coupling in copper.

Our RSGF simulations use XAS from 20 atomic configurations taken from QMD calculations using the VASP code [36,37] with generalized gradient approximation (GGA) exchange-correlation potentials [38]. We also used the projector augmented wave (PAW) potentials with an energy cutoff of 590 eV. The system with a $2 \times 2 \times 2$ supercell constructed from a conventional unit cell of eight atoms is propagated with a time step of 1 fs to reach equilibration, and the sampling of configurations is performed by randomly sampling from a 2-ps-long trajectory with a time step of 1 fs. We compare our simulation at temperatures $T_e = 300$, 10 200, and 6000 K for the time delays $t < 0$ ps, $t = 2$ ps, and $t = 9$ ps, respectively, with those from DFT-based calculations [4] in Fig 8. Note that our calculation underestimates the Fermi level for $T_e = 10\,200$ K ($t = 2$ ps) by a few eV, leading to the observed shift in the XANES.

C. Transition metals: Ti and Au

As examples of other finite electronic-temperature L_3-edge XAS calculations, we present FT calculations for an early transition metal (hcp titanium), where the d bands are partially filled, and for a late transition metal (fcc gold) where the d bands are full, both at normal density. Figure 9 shows the electronic-temperature dependence of the L edges of these materials due to the FT SCF, FT exchange-correlation potential, $v_{\mathrm{xc}}^{\mathrm{KSDT}}$, and the Fermi function smearing in the cross section. The XANES of Ti is blueshifted with increasing electronic temperature because the chemical potential is located in the middle of the d band and the density of states above the chemical potential is higher. Also, the Fermi-Dirac distribution in the cross section broadens with increasing temperature leading to the broader structure above the edge as more d states are included in the transition.

In contrast, the XANES of gold (Au) is redshifted, as shown in bottom plot of Fig. 9. This opposing behavior in Ti and Au is due to the higher density of states below the chemical potential. Again, the onset of the pre-edge structure is due to the broadening of the Fermi-Dirac distribution and shift of the chemical potential. Unlike Ti, the broadening of the Fermi-Dirac distribution does not alter the XANES above the edge because the localized d band is well below the Fermi level.

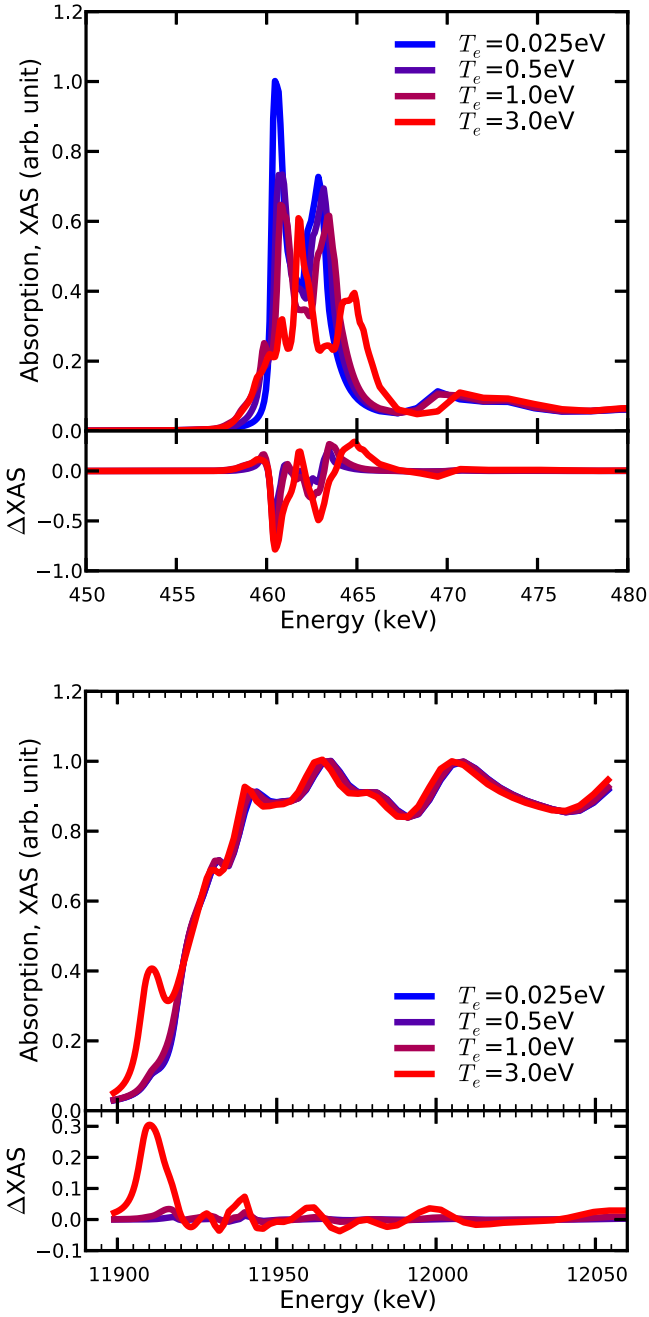

FIG. 9. L_3-edge absorption for hcp titanium (top) where the XAS reflects that of the unfilled d bands, and gold (bottom) where the d bands are nearly filled. The difference ΔXAS between the XAS at finite T_e and zero temperature is also shown.

D. MgO

As a final example, we present results for the Mg K-edge XANES of MgO at normal density with FT lattice behavior calculated using the quasiharmonic approximation. While our calculation accounts for most of the FT effects discussed in Sec. III (excluding the temperature dependence of the self-energy), the important effects for the temperature range considered here are the FT SCF, the Fermi function in the cross section, and vibrational effects.

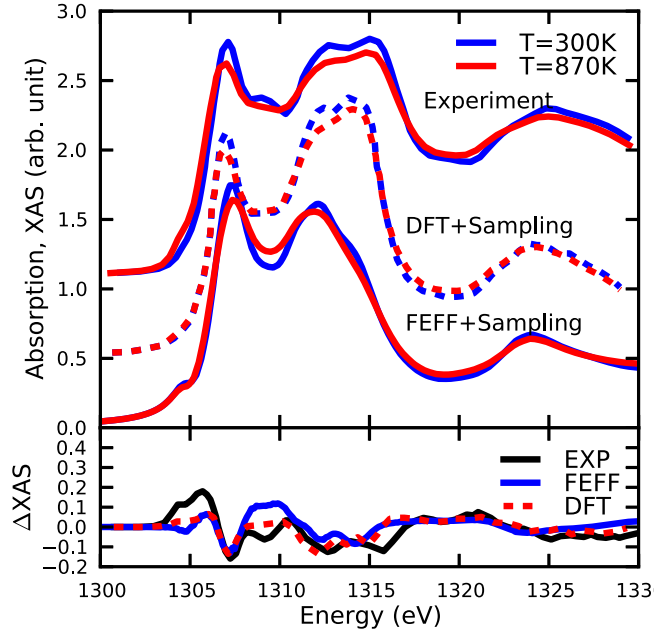

FIG. 10. Mg K-edge spectra for MgO at temperature $T = 300$ K (blue) and 870 K (red). The top plot shows the experimental spectra [39], the DFT spectra [39], and the FEFF quasiharmonic spectra. The bottom plot shows the spectra difference with respect to $T = 300$ K for the experiment (solid black), FEFF (solid blue), and DFT (dashed red) are shown.

Figure 10 shows the average XAS for 30 randomly sampled configurations at equilibrium temperatures $T_e = T_L = 300$ and 870 K. The configurations are obtained by sampling the normal modes calculated from dynamical matrices at the experimental lattice constants and the given temperatures using QUANTUM ESPRESSO code [40–42], with GGA functional [43] for a 16-atom $2 \times 2 \times 2$ supercell constructed from a two-atom primitive cell. The electronic density of state is computed with a $6 \times 6 \times 6$ k-point grid with an energy cutoff of 58 Ry. Next, we use the density-functional perturbation theory to compute the dynamical matrix calculation at the Γ point. The long-range electric fields are accounted for from the calculation of the Born effective charge.

FEFF calculations have been found to overestimate the screening effect of light element oxides [44]. Instead of using the *ad hoc* $Z + 1$ approach to overcome the strong screening effect of the final state rule, we used the random-phase approximation (RPA) for the core-hole screening in FEFF. The RPA is more accurate in this case, being similar to a Bethe-Salpeter equation [45,46]. Finally, we add an additional energy shift of 2.6 eV to the chemical potential. As a comparison, we show the experiment and DFT calculation by Nemausat emphet al. using the stochastic self-consistent harmonic approximation [39] in Fig. 10. The decrease in the absorption amplitude is due to the lattice vibration similar to the examples previously shown. Our model underestimates the excitations between the energy range 1310 and 1315 eV. This can be attributed to the spherical muffin-tin potential approximation used in our calculations.

V. SUMMARY AND CONCLUSIONS

We have extended the real-space Green's function theory of XAS [23] to high temperatures (HT) from about T_D up to the warm dense matter regime $T \approx T_F$. This generalization takes into account both electronic-temperature and lattice-temperature effects, which are particularly important at HT. Briefly, a finite-temperature (FT) SCF procedure is carried out in the complex energy plane in terms of the FT one-electron Green's function. This leads to a decrease in the chemical potential with increasing temperature, i.e., "continuum lowering," uncovering contributions to the pre-edge spectra below the $T = 0$ Fermi level. This SCF procedure includes the FT exchange-correlation potential, which is approximated here using the KSDT parametrization. An important difference from the $T = 0$ theory of XAS is the smearing of the absorption edge and the presence of peaks below the $T = 0$ Fermi energy in the spectra due to FT occupation numbers. The finite-temperature exchange-correlation potential has a small effect on XAS when $T \ll T_F$ compared to the Fermi smearing. The self-energy is also important for XAS, accounting for shifts and final-state broadening; at HT the effect adds a small but non-negligible increase in broadening that is only weakly energy dependent. While dynamic exchange effects can also be included, due to the difficulty of their calculation, a more efficient COHSEX approximation can be used. At low T vibrational effects can be included in terms of a correlated Debye model, but need to be replaced by a configurational average at high T for XANES. The FT and HT generalizations introduced here are implemented as an extension of the FEFF codes in a new version FEFF10 [20].

Our approach for HT XAS has been tested against various experiments, and typically yields good overall agreement. We find that the most important effects on the spectrum are due to (1) the smearing of the Fermi function in the calculation of the cross section; (2) the shift in the chemical potential due to the finite-temperature SCF; and (3) the damping of fine structure due to lattice vibrations. The relative importance of these effects changes, depending on the system, energy range, and state of equilibrium in question. We believe these developments may be useful in interpretation of many experiments, e.g., for studies of nonequilibrium behavior, extreme conditions, and shocked conditions. The approach can also be used to differentiate between lattice- and electronic-temperature effects.

ACKNOWLEDGMENTS

We thank R. Albers, B. Fultz, D. Prendergast, G. Seidler, S. Trickey, F. Vila, and H. Wende for comments and suggestions. This work is supported by DOE BES Grant No. DE-FG02-97ER45623. The development of FEFF10 was carried out within the Theory Institute for Materials and Energy Spectroscopies (TIMES) at SLAC, and is supported by the U.S. DOE, Office of Basic Energy Sciences, Division of Materials Sciences and Engineering, under Contract No. DE-AC02-76SF00515.

[1] A. Savin, Shelley L. P. Berko, A. N. Blacklocks, W. Edwards, and A. V. Chadwick, C. R. Chim. **11**, 948 (2008).
[2] G. J. Sherborne and B. N. Nguyen, Chem. Cent. J. **9**, 37 (2015).
[3] F. Lin, Y. Liu, X. Yu, L. Cheng, A. Singer, O. G. Shpyrko, H. L. Xin, N. Tamura, C. Tian, T.-C. Weng, X.-Q. Yang, Y. S. Meng, D. Nordlund, W. Yang, and M. M. Doeff, Chem. Rev. **117**, 13123 (2017).
[4] B. I. Cho, K. Engelhorn, A. A. Correa, T. Ogitsu, C. P. Weber, H. J. Lee, J. Feng, P. A. Ni, Y. Ping, A. J. Nelson, D. Prendergast, R. W. Lee, R. W. Falcone, and P. A. Heimann, Phys. Rev. Lett. **106**, 167601 (2011).
[5] C. Stamm, N. Pontius, T. Kachel, M. Wietstruk, and H. A. Dürr, Phys. Rev. B **81**, 104425 (2010).
[6] R. Bolis, J.-A. Hernandez, V. Recoules, M. Guarguaglini, F. Dorchies, N. Jourdain, A. Ravasio, T. Vinci, E. Brambrink, N. Ozaki, J. Bouchet, F. Remus, R. Musella, S. Mazevet, N. J. Hartley, F. Guyot, and A. Benuzzi-Mounaix, Phys. Plasmas **26**, 112703 (2019).
[7] R. M. Martin, L. Reining, and D. M. Ceperley, *Interacting Electrons: Theory and Computational Approaches* (Cambridge University Press, New York, 2016).
[8] D. Prendergast and G. Galli, Phys. Rev. Lett. **96**, 215502 (2006).
[9] C. E. Starrett, Phys. Rev. E **97**, 053205 (2018).
[10] C. E. Starrett and N. Shaffer, Phys. Rev. E **102**, 043211 (2020).
[11] M. Laraia, C. Hanson, N. R. Shaffer, D. Saumon, D. P. Kilcrease, and C. E. Starrett, High Energy Density Phys. **40**, 100940 (2021).
[12] J. J. Rehr, J. J. Kas, F. D. Vila, M. P. Prange, and K. Jorissen, Phys. Chem. Chem. Phys. **12**, 5503 (2010).
[13] R. Zeller, J. Deutz, and P. Dederichs, Solid State Commun. **44**, 993 (1982).
[14] K. Wildberger, P. Lang, R. Zeller, and P. H. Dederichs, Phys. Rev. B **52**, 11502 (1995).
[15] J. Staunton, B. Gyorffy, A. Pindor, G. Stocks, and H. Winter, J. Phys. F: Met. Phys. **15**, 1387 (1985).
[16] H. Ebert, D. Koedderitzsch, and J. Minar, Rep. Prog. Phys. **74**, 096501 (2011).
[17] J. Minár, L. Chioncel, A. Perlov, H. Ebert, M. I. Katsnelson, and A. I. Lichtenstein, Phys. Rev. B **72**, 045125 (2005).
[18] J. J. Kas, T. D. Blanton, and J. J. Rehr, Phys. Rev. B **100**, 195144 (2019).
[19] J. Minár, O. Ŝipr, J. Braun, and H. Ebert, *Multiple Scattering Theory for Spectroscopies*, edited by D. Sébilleau, K. Hatada, and H. Ebert, Springer Proceedings in Physics, Vol. 204 (Springer, Cham, 2018), pp. 93–142.
[20] J. J. Kas, F. D. Vila, C. D. Pemmaraju, T. S. Tan, and J. J. Rehr, arXiv:2106.13334 [cond-mat.mtrl-sci].
[21] J. J. Rehr and R. C. Albers, Phys. Rev. B **41**, 8139 (1990).
[22] J. J. Kas, J. J. Rehr, and J. B. Curtis, Phys. Rev. B **94**, 035156 (2016).
[23] J. J. Rehr and R. C. Albers, Rev. Mod. Phys. **72**, 621 (2000).
[24] A. L. Ankudinov, B. Ravel, J. J. Rehr, and S. D. Conradson, Phys. Rev. B **58**, 7565 (1998).
[25] V. V. Karasiev, T. Sjostrom, J. Dufty, and S. B. Trickey, Phys. Rev. Lett. **112**, 076403 (2014).

[26] J. J. Kas and J. J. Rehr, Phys. Rev. Lett. **119**, 176403 (2017).
[27] T. S. Tan, J. J. Kas, and J. J. Rehr, Phys. Rev. B **98**, 115125 (2018).
[28] F. D. Vila, V. E. Lindahl, and J. J. Rehr, Phys. Rev. B **85**, 024303 (2012).
[29] U. v. Barth and L. Hedin, J. Phys. C: Solid State Phys. **5**, 1629 (1972).
[30] Z. Lin, L. V. Zhigilei, and V. Celli, Phys. Rev. B **77**, 075133 (2008).
[31] A. Manãić, A. Lévy, M. Harmand, M. Nakatsutsumi, P. Antici, P. Audebert, P. Combis, S. Fourmaux, S. Mazevet, O. Peyrusse, V. Recoules, P. Renaudin, J. Robiche, F. Dorchies, and J. Fuchs, Phys. Rev. Lett. **104**, 035002 (2010).
[32] B. I. Cho, T. Ogitsu, K. Engelhorn, A. A. Correa, Y. Ping, J. W. Lee, L. J. Bae, D. Prendergast, R. W. Falcone, and P. A. Heimann, Sci. Rep. **6**, 18843 (2016).
[33] B. Mahieu, N. Jourdain, K. Ta Phuoc, F. Dorchies, J.-P. Goddet, A. Lifschitz, P. Renaudin, and L. Lecherbourg, Nat. Commun. **9**, 3276 (2018).
[34] N. Jourdain, L. Lecherbourg, V. Recoules, P. Renaudin, and F. Dorchies, Phys. Rev. B **97**, 075148 (2018).
[35] N. Jourdain, V. Recoules, L. Lecherbourg, P. Renaudin, and F. Dorchies, Phys. Rev. B **101**, 125127 (2020).
[36] G. Kresse and J. Furthmüller, Phys. Rev. B **54**, 11169 (1996).
[37] G. Kresse and D. Joubert, Phys. Rev. B **59**, 1758 (1999).
[38] J. P. Perdew, K. Burke, and M. Ernzerhof, Phys. Rev. Lett. **77**, 3865 (1996).
[39] R. Nemausat, D. Cabaret, C. Gervais, C. Brouder, N. Trcera, A. Bordage, I. Errea, and F. Mauri, Phys. Rev. B **92**, 144310 (2015).
[40] P. Giannozzi, S. Baroni, N. Bonini, M. Calandra, R. Car, C. Cavazzoni, D. Ceresoli, G. L. Chiarotti, M. Cococcioni, I. Dabo, A. Dal Corso, S. de Gironcoli, S. Fabris, G. Fratesi, R. Gebauer, U. Gerstmann, C. Gougoussis, A. Kokalj, M. Lazzeri *et al.*, J. Phys.: Condens. Matter **21**, 395502 (2009).
[41] P. Giannozzi, O. Andreussi, T. Brumme, O. Bunau, M. B. Nardelli, M. Calandra, R. Car, C. Cavazzoni, D. Ceresoli, M. Cococcioni, N. Colonna, I. Carnimeo, A. D. Corso, S. de Gironcoli, P. Delugas, R. A. D. Jr, A. Ferretti, A. Floris, G. Fratesi, G. Fugallo *et al.*, J. Phys.: Condens. Matter **29**, 465901 (2017).
[42] P. Giannozzi, O. Baseggio, P. Bonfà, D. Brunato, R. Car, I. Carnimeo, C. Cavazzoni, S. de Gironcoli, P. Delugas, F. Ferrari Ruffino, A. Ferretti, N. Marzari, I. Timrov, A. Urru, and S. Baroni, J. Chem. Phys. **152**, 154105 (2020).
[43] We used the pseudopotentials Mg.pbesol-spnl-kjpaw_psl.1.0.0.UPF and O.pbesol-n-kjpaw_psl.1.0.0.UPF from http://www.quantum-espresso.org.
[44] K. Nakanishi and T. Ohta, J. Phys.: Condens. Matter **21**, 104214 (2009).
[45] A. L. Ankudinov, A. I. Nesvizhskii, and J. J. Rehr, Phys. Rev. B **67**, 115120 (2003).
[46] J. J. Rehr, J. A. Soininen, and E. L. Shirley, Phys. Scr. **T115**, 207 (2005).